



Conformal formation of Carbon-TiO_x matrix encapsulating silicon for high-performance lithium-ion battery anode



Kun Feng^a, Matthew Li^a, Heywoong Park^a, Gregory Lui^a, Wenwen Liu^a, Ali Ghorbani Kashkooli^a, Xingcheng Xiao^{b,*}, Zhongwei Chen^{a,*}

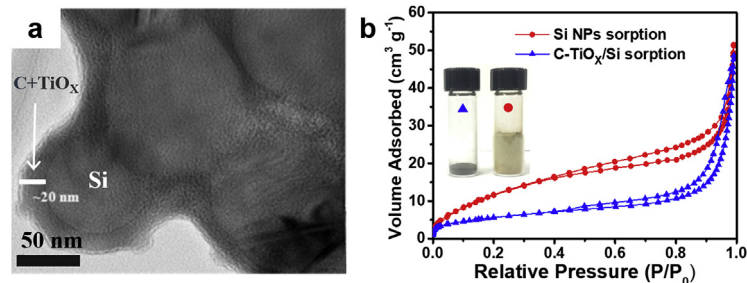
^a Department of Chemical Engineering, Waterloo Institute for Nanotechnology, Waterloo Institute of Sustainable Energy, University of Waterloo, 200 University Ave. W, Waterloo, ON, N2L 3G1, Canada

^b General Motors Global Research and Development Center, 30500 Mound Road, Warren, MI, 48090, United States

HIGHLIGHTS

- Controllable conformal formation of C-TiO_x coating matrix for Si is developed.
- Amorphous TiO_x coating contributes to better cycling stability and rate performance.
- Formation of micron-sized clusters greatly enhances the tap density of Si NPs.

GRAPHICAL ABSTRACT



ARTICLE INFO

Keywords:

Silicon-based anode
Conformal formation
TiO_x
Lithium-ion battery
Micron-sized cluster

ABSTRACT

Nanonization strategies are effective in preventing silicon anodes from pulverization and reducing the required diffusion lengths of lithium ions inside silicon structure, and thus obtain improved cycling performance over bulky silicon. However, new problems arise with nano silicon, such as reduced tap density, larger specific surface area, and poorly percolating conductive paths in electrodes. These new issues can result in reduced volumetric energy densities, unstable solid electrolyte interphase, increased irreversible capacities and low Coulombic efficiencies. This study introduces an effective strategy in harvesting the benefits of nano silicon, while eliminating the unfavorable phenomena that arise from nanonization. A novel micron-sized secondary cluster with silicon nanoparticles embedded in an amorphous carbon and TiO_x matrix is developed. The matrix is conformally formed on the surface of silicon, which not only uniformly casts a protective layer on silicon, but also integrates nano silicon into micron clusters. The secondary cluster exhibits much improved tap density over silicon nanoparticles. The amorphous and defect-rich nature of the TiO_x coating not only exhibits enhanced electronic conductivity over its crystalline counterparts, but also provides better elasticity and stress-release capability that can maintain the structural integrity over lithiation/delithiation of silicon. Direct and repetitive contact between silicon and electrolyte is prevented and thus formation of a stable solid electrolyte interphase is facilitated. Half-cell batteries made with the composite exhibit an initial capacity of 1410 mA g⁻¹ at a current density of 100 mA g⁻¹, and display stable long-term cycling with ~88% capacity retention after 200 cycles at 1 A g⁻¹.

* Corresponding author.

** Corresponding author.

E-mail addresses: xingcheng.xiao@gm.com (X. Xiao), zhwchen@uwaterloo.ca (Z. Chen).

1. Introduction

Silicon (Si) is the most promising candidate as anode material for next-generation lithium-ion batteries (LIBs) due to its superior capability in reversible lithium storage, high abundance, low cost, and good environmental friendliness. Compared to its widely commercialized graphite counterpart, which only exhibits a theoretical capacity of 372 mAh g⁻¹, Si bears over ten-fold the capacity (4200 mAh g⁻¹) of graphite, upon full lithiation and formation of Li₂₂Si₅ alloy [1–3]. However, large volume change occurs during the alloying and dealloying process, easily causing cracks on bulky Si and eventually pulverizing the material over prolonged cycling. This intrinsic volume change not only breaks down Si structure and disrupts electron conductive paths in the electrode, but also constantly damages the solid electrolyte interphase (SEI) that forms on the surface of Si and exposes fresh surfaces to electrolyte for unstable SEI to propagate [4,5]. A stable SEI is crucial to the steady cycling of Si as it self-passivates on the surface of active material in initial cycles and prevents further direct contact between electrolyte and active material, and thus avoids excessive SEI formation and benefit electrode structural stability. Repetitive SEI growth isolates Si from conductive network in electrode and deactivates Si. Furthermore, Li ions in electrolyte are constantly consumed which leads to irreversible capacities. All these problems contribute to the capacity loss and electrode failure over cycling [6].

To tackle the above-mentioned problems with Si electrodes, many efforts have been devoted to the development of Si nanostructures and Si-based composites. Various Si nanostructures, including nanowires [7,8], nanotubes [9], thin films [10], have been exploited to provide robust mechanical properties and circumvent structure failure patterns. They have been proven effective in alleviating the degeneration of Si structures. In addition to the shortened Li-ion diffusion path and robust stress relaxation in nanostructured Si, it was later discovered that the pulverization does not occur once Si is engineered to be below a critical dimension [11]. Driven by these unique properties, research on nano Si has flourished and is continuing as a major research direction. Meanwhile, researchers have realized that nanonization is not the panacea to all the problems associated with Si anodes. One obvious drawback with engineering complex nanostructures is the daunting cost spike, which prevents their wide commercial application [12,13]. Another issue is the significantly increased specific area, which provides more contact between electrode and electrolyte, making it difficult for a stable SEI to form [14]. Even worse, nanonization inevitably reduces the tap density of Si, which is unfavorable of the high-energy-density demand for LIBs [15,16]. Many types of carbon materials have been adopted to composite with Si and provide enhanced cycling performance. Much improved electronic conductivity of electrode material can be achieved by embedding Si into a carbon matrix [17].

Titanium-based materials have been proposed as a group of benign and safe electrode materials in the application of LIBs due to the non-toxic nature of titanium element [18,19]. TiO₂ have been reported as both an electrode material and coating/stuffing/skeleton material in Si-based composites [20,21]. TiO₂ experiences less drastic volume change than Si during lithiation/delithiation process. Other than that, the charge and discharge plateau of TiO₂ (above 1.5 V vs. Li/Li⁺) is much higher than that of Si [22]. One can easily tune the charge and discharge window of a battery with TiO₂/Si anode so that TiO₂ remains at lithiated state over cycling, without repetitive lithiation of TiO₂. TiO₂ is more thermally stable when compared to its carbon counterparts, and thus improves safety of batteries in the case of a thermal runaway [23]. Many types of TiO₂/Si hybrids have been developed via different synthetic routes. There are generally two approaches of combining Si and TiO₂. One is to have TiO₂ coating on Si structures, and the other one is to employ TiO₂ as template for Si deposition/growth [24,25]. Nanostructures that have been reported in both approaches include nanowires, nanotubes, nanoparticles [26,27]. Despite the benefits of TiO₂, one must note that TiO₂ has a low electronic conductivity

(< 10⁻⁴ S cm⁻¹), which has been used as an insulator at room temperature [28].

To fully harvest the benefits of compositing Si with TiO₂, a carbon-coated TiO_x matrix with Si NPs embedded inside is prepared via a facile synthetic strategy, which not only circumvents the disadvantages of both, but also organically utilizes the advantages of nano-sized Si. Si NPs are firstly coated with a layer of TiO₂ and meanwhile form micron-sized clusters. To enhance the electronic conductivity and improve the mechanical robustness of the TiO₂ coating layer, the preliminary composite is subsequently annealed at an elevated temperature in a reducing atmosphere to partially reduce the TiO₂ to TiO_x where x is between 0 and 2. In the same annealing step, a carbon-containing precursor gas is introduced in the end, which decomposes and forms a thin carbon coating layer on TiO_x/Si clusters, after which the C-TiO_x/Si composite is obtained. In the created cluster, C-TiO_x acts as a hosting matrix for Si NPs, and thus provide a stable scaffold for the latter. In this sense, the dedicated coating physically suppresses interparticle interactions and avoids unregulated agglomeration of Si NPs. This C-TiO_x/Si composite not only bears the benefits of Si NPs, such as good volume change adaption, shortened Li-ion diffusion and electron conduction paths, but also decreases the specific surface area and improves the tap density of Si. Tap density of the new composite is over four time that of Si NPs. Deliberately tailored and hydrogenated TiO_x matrix can act as a protective coating on Si, avoiding excessive SEI formation, and a buffer matrix that holds together Si NPs and absorb volume change of Si from lithiation/delithiation process. Another carbon coating layer further enhances the conductivity of the composite and ensures sufficient effective contact points between the cluster and conductive network in electrode. Overall, this cluster composite not only provides a matrix that encapsulates Si NPs, but also has excellent electrical conductivity that facilitates fast electrochemical reaction in the electrode. The protective TiO_x coating layer, as well as the reduced specific surface area can contribute to a more stable SEI that ensures long-term reversible Li storage. Moreover, the formation of micron-sized secondary cluster effectively increases the tap density of the composite over Si NPs, offsetting the drawback from nanonization, and paving way for practical application of Si anodes.

2. Experimental methods

2.1. Material Synthesis

In a typical synthesis process, 400 mg of Si NPs (NanoAmor, $\phi \sim 70$ nm) and 120 ml of anhydrous ethanol were sonicated in a round-bottom flask for 2 h for Si NPs to disperse in ethanol. After that, 800 μ L of titanium n-butoxide (TBOT) (Sigma Aldrich) was added into the flask and stirred for 30 min, followed by dropwise addition of 800 μ L distilled deionized water (DDI) over 15 min period. The mixture was refluxed and stirred at 90 °C in an oil bath for 6 h before it was removed from the set-up and naturally cooled down. The sample was washed, dried and weighed. The intermediate TiO₂/Si product of around 600 mg can be obtained from each batch. TiO₂/Si was subsequently placed in a tube furnace for the final formation step of TiO_x and carbon coating. Temperature of the furnace was first elevated to 800 °C and maintained for 2 h for TiO₂ phase stabilization in an argon atmosphere. Ten percent H₂ in Ar was subsequently passed through the quartz tube to hydrogenate TiO₂ and create oxygen deficiencies in TiO₂. Finally, toluene vapor was introduced to the system for a short period of time (15 min) for the deposition of carbon. Si/C composite without the inclusion of TiO_x matrix was prepared according to the same procedure of C-TiO_x/Si, except for the addition of TBOT. C-TiO₂/Si was prepared following the same synthetic route of C-TiO_x/Si, except for the H₂ introduction during annealing.

2.2. Physical characterization

Morphologies of the samples were obtained from scanning electron microscope (SEM, Zeiss Ultra Plus field emission microscope), and transmission electron microscope (TEM, JEOL, 2010F TEM/STEM field emission microscope) featured with high-resolution capability and equipped with an energy-dispersive X-ray spectroscopy (EDX). X-ray diffraction (XRD) patterns were obtained from an Inel XRG 3000 diffractometer (monochromatic Cu K X-rays, 0.154 nm). X-ray photoelectron spectroscopy (XPS, Thermo Scientific K-Alpha) was conducted to measure the surface properties of samples and oxidation states of elements. Thermal gravimetric analysis was carried out in air atmosphere. The nitrogen adsorption isotherms were obtained from a surface area and porosimetry system (Micromeritics ASAP, 2020 Plus), with over 3 h degassing at a temperature of 250 °C.

2.3. Electrochemical measurements

The composition of all working electrodes in this research was as follows: 80% active material, 10% Super-P conductive carbon, and 10% sodium carboxymethyl cellulose (CMC) binder (In 2% water solution). Height between the casting doctor blade and copper foil was maintained at 120 μm for all electrodes. Same pressure of 200 pounds per cm² was applied to press all electrodes. Working electrodes were paired with Li counter electrodes and made into CR2032-type coin cells for all electrochemical measurements. All battery-assembly parts and materials were thoroughly dried before being transferred into an argon-filled glovebox (Labstar 10, Mbraun) for cell assembly. Only one type of electrolyte was used in this research, and the composition was 1 M LiPF₆ in a solution mixture of ethylene carbonate (EC), dimethyl carbonate (DMC), and fluoroethylene carbonate (FEC) (45:45:10, by volume, BASF). Separator placed in between cathode and anode was a polypropylene membrane from Celgard (PP2500, high porosity, 25 μm microporous). Galvanostatic charge/discharge tests were performed on battery testers from Neware, with voltage range from 0.05 to 1.5 V. Rate capability and long-term cycling stability of each material were obtained from the charge/discharge tests. Potentiostatic electrochemical impedance spectroscopy (EIS) data were collected on an electrochemical workstation (Versa Stat MC, Princeton Applied Research). EIS was conducted in the frequency range of 1 M–0.1 Hz, with a perturbation voltage amplitude of 10 mV.

3. Results and discussion

A carbon-coated TiO_x matrix with Si NPs embedded inside is prepared by a two-step synthesis process as shown in the schematic in Fig. 1a. Si NPs are firstly well dispersed and dissociated in ethanol under reflux. Titanium n-butoxide (TBOT) is subsequently added so that surface of Si NPs is enriched with TBOT molecules. With the addition of water, TBOT hydrolyses and forms the coating layer on Si NPs. Meanwhile, secondary clusters are generated. The intermediate product is obtained after washing and drying, and is later placed in a tube furnace for the subsequent phase stabilization, oxygen deficiency creation, and carbon coating. Details of a typical synthesis are described in the Material Synthesis section. The micron-sized secondary cluster composite is obtained and denoted as C-TiO_x/Si. Discrete Si NPs agglomerate into micron-sized clusters after the synthesis (Fig. 1b and c). As shown in Fig. 1d, Si NPs are firmly attached to the secondary cluster with no dissociated Si NPs. Homogeneous C and TiO_x coating can be clearly observed in the TEM image shown in Fig. 1e. Thickness of the C and TiO_x layers are measured to be ~5 nm and ~15 nm respectively. Fig. 1f is a scanning TEM (STEM) image of the edge of a C-TiO_x/Si particle, with focus on the bulge of a single Si NP. Elemental mappings of the highlighted area are displayed in Fig. 1g–j, representing elements of C, O, Si, and Ti respectively. It is interesting to note that Si is universally covered by C and titanium oxide layers. Si and Ti elemental

mappings display a clear contrast, highlighting the shape of the Si core and the TiO_x shell.

By tuning the ratio of Ti source to Si during the synthesis, amount of TiO_x and the final thickness of the TiO_x coating can be controlled. In addition to the C-TiO_x/Si composite which utilizes TBOT:Si mass ratio of 2:1, different thicknesses are obtained when TBOT:Si mass ratios are changed to 4:1 and 1:1. With an initial TBOT:Si mass ratio of 4:1, thickness of the TiO_x layer is ~30 nm, while the TiO_x coating layer prepared with TBOT:Si mass ratio of 1:1 is mere ~5 nm (Figure S1). Excess TiO₂ can be seen existing as small particles, in addition to coatings on Si, when TBOT:Si mass ratio of 4:1 is used (Figure S2). Only a very thin layer of TiO₂ (~5 nm) can be observed when the ratio of TBOT to Si is 1:1. The TiO_x/Si structure is not well integrated, with some Si NPs dissociated beyond the cluster structure (Figure S3). Reflux reaction condition is also a vital factor to the homogeneous coating of TiO_x layer, as it significantly enhances the dispersion of reactants and promotes uniform coating. SEM images of a TiO_x/Si sample prepared under the same condition except for the missing of reflux show that significant amount of TiO_x tends to form particles (Figure S4), instead of uniformly coating on Si NPs.

XRD experiments were conducted to investigate the crystallinity changes during different stages of the synthesis. As shown in Fig. 2a, distinct Si peaks can be observed with pure Si NPs. After the first TiO₂ coating process, anatase TiO₂ phase appears in the diffraction pattern, in addition to the original Si peaks (Figure S5). After heat treatment at 800 °C, it is apparent that Si maintains its crystalline phase, while the crystallinity of TiO₂ is decreased, as indicated by the shorter and broader [101] peak at 25.6°. After the carbon coating process, no distinct carbon peaks are generated, indicating the amorphous nature of the carbon coating layer. Without hydrogen treatment, the anatase phase of TiO₂ remains after the carbon coating process. In contrast, the anatase peaks of TiO₂ disappear in C-TiO_x/Si after hydrogen treatment, revealing the significant decrease in crystallinity, consistent with previous studies with TiO₂ [29]. XPS is carried out to further study the effect of hydrogen treatment on the properties of titanium oxide layer. As shown in Fig. 2b, a brief shift (–0.3 eV) in the binding energies of Ti 2p_{1/2} and Ti 2p_{3/2} peaks in C-TiO_x/Si compared to the pristine anatase TiO₂ confirms the partial reduction of Ti⁴⁺ and creation of oxygen vacancies in the titanium oxide layer [30]. A higher density of charge carriers can be achieved as a result of the generation of oxygen vacancies, which can be translated to the enhanced electron conductivity of the synthesized material [31]. In the O 1s XPS spectra displayed in Fig. 2c, characteristic Ti-O-Ti XPS peak of O 1s spectra can be clearly identified at ~530.5 eV. A broad peak centering at 531.6 eV can be attributed to the Ti-O-H bond created by the hydrogenation [32]. The existence of SiO₂ is also revealed by the Si-O-Si peak at ~532.9 eV. TGA is conducted in air with C-TiO_x/Si, C-TiO₂/Si, and C/Si samples. Contents of carbon can be readily observed to be in the range of 13–16% among the three samples (Fig. 2d), which indicates the good reproductivity of carbon coating with same reaction condition applied. It is noteworthy to mention the weight increase of C-TiO_x/Si sample which commences at around 250 °C. This phenomenon can be ascribed to the saturation of oxygen in TiO_x and formation of TiO₂. TiO_x synthesized via an identical hydrogenation process displays a similar weight increase pattern over the same temperature range in TGA profile (Figure S6) with C-TiO_x/Si. This weight gain is absent in the C/Si profile, proving the sole contribution from TiO_x. The weight increase with C/Si after 600 °C can be attributed to the oxidation of Si, which is barely visible from the C-TiO_x/Si profile, proving the uniform coating of titanium oxide layer that effectively slows Si from being oxidized by the oxidizing atmosphere. Formation of the integrated Si-based cluster increases the tap density of Si. Photographs of two vials (Figure S7) containing the same mass of materials (0.4 g) provide a distinct comparison of the C-TiO_x/Si and pristine Si NPs. Tap density increases from 0.18 g cm⁻³ for Si NPs to 0.88 g cm⁻³ for the micron-sized composite. Nitrogen adsorption/desorption isotherms of C-TiO_x/Si and Si NPs are

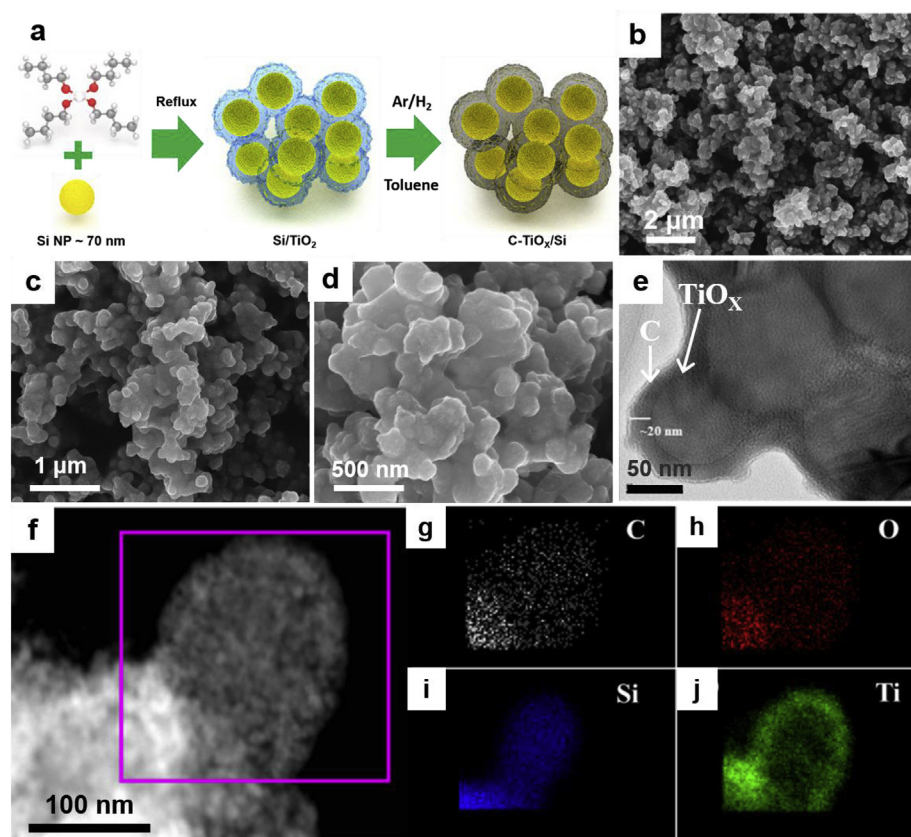


Fig. 1. a) Schematic illustration of the synthetic procedure of C-TiO_x/Si, b-d) C-TiO_x/Si cluster at magnifications of 20,000 \times , 50,000 \times , and 100,000 \times , respectively. e) TEM image with focus on a few Si NPs on C-TiO_x/Si, f) STEM image with focus on a single Si NP, g-j) C, O, Si, and Ti elemental mappings of the highlighted area in f).

displayed in Fig. 2e. The BET surface areas of C-TiO_x/Si and Si NPs are discovered to be 13.44 and 76.68 m² g⁻¹, respectively. A clear decrease in the specific surface area is observed after the synthesis. This result is consistent with previous studies stating that increase of particle size dramatically changes the specific surface area and volumetric density of a material [33,34].

Galvanostatic charge and discharge tests are performed on cells with C-TiO_x/Si and C-TiO₂/Si, respectively. Voltage window of the cells is set to be 0.05–2.5 V in the first three cycles to study the Li⁺ insertion/extraction behaviors of the materials. As shown in Fig. 3a and b, an apparent voltage plateau burgeoning from above 0.6 V can be ascribed

to the formation of SEI in the C-TiO_x/Si cell. Both C-TiO₂/Si and C/Si cells experience similar SEI formation process in their first discharge. Like many other anodes that have been reported, this plateau is universal in anode materials that have half-cell discharge potential below 1 V. The charge profiles of all three materials are featured with extensive capacity contributions from voltage range from 0.05 to 0.6 V, which is the characteristic Li⁺ extraction potential of Si. One distinct difference of the profiles between the C-TiO_x/Si and C-TiO₂/Si cells lies at \sim 2.02 V, where the latter displays a clear plateau, arising from the characteristic extraction behavior of Li⁺ from the octahedral sites of the crystalline anatase TiO₂ [35]. This plateau is almost invisible in the C-

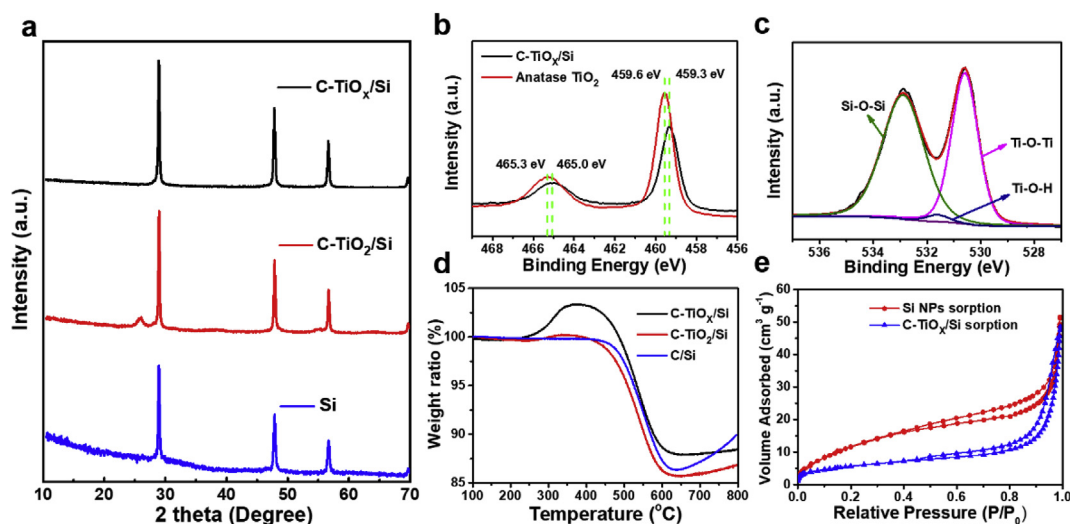


Fig. 2. a) XRD patterns of Si, C-TiO₂/Si, and C-TiO_x/Si, b) Ti 2p high-resolution XPS spectra of C-TiO_x/Si and anatase TiO₂, c) O 1s high-resolution XPS spectrum of C-TiO_x/Si, d) TGA graphs of C/Si, C-TiO₂/Si, and C-TiO_x/Si, e) nitrogen sorption isotherms of Si and C-TiO_x/Si.

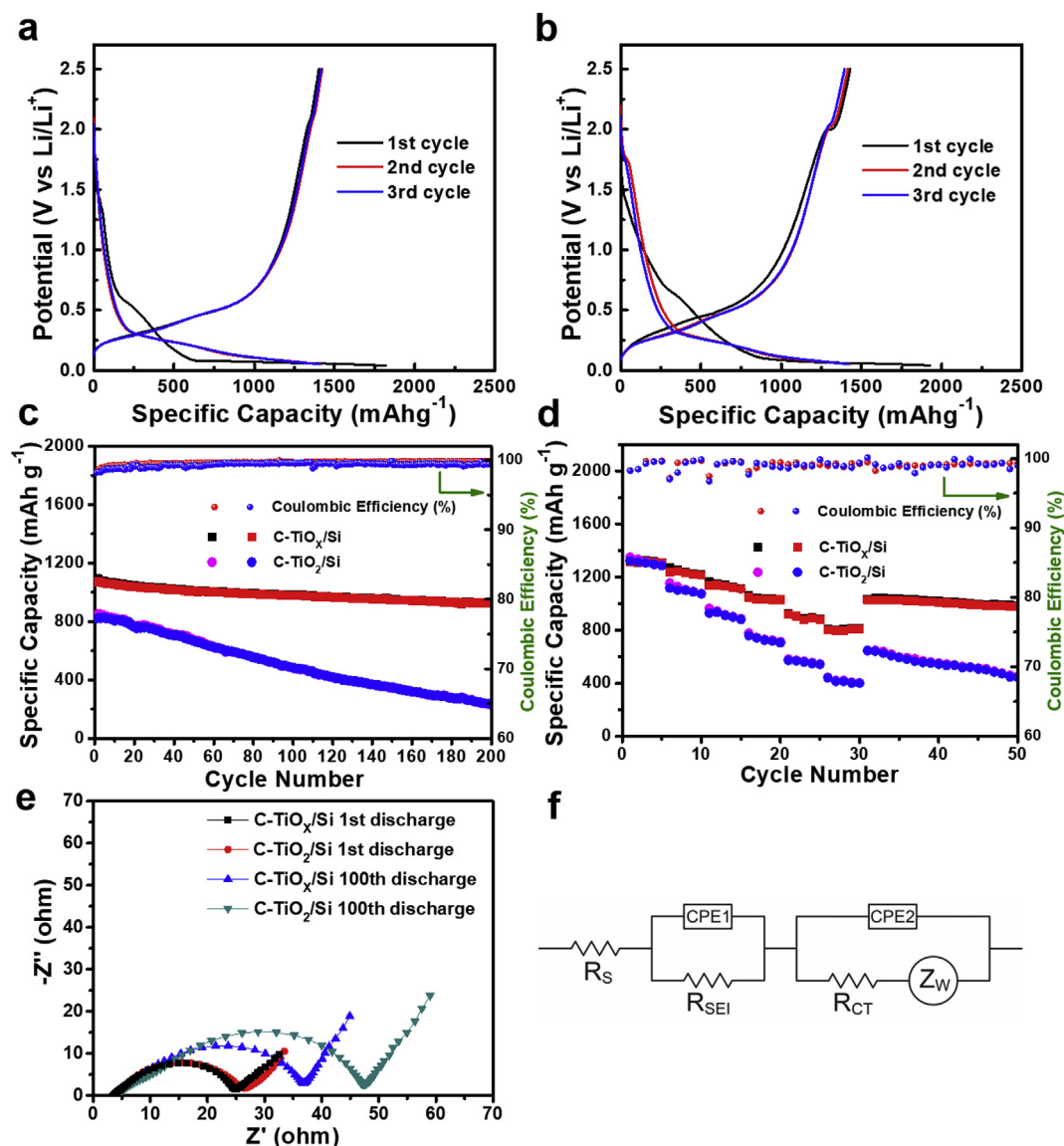


Fig. 3. Voltage profiles of a) C-TiO_x/Si and b) C-TiO₂/Si for first three cycles at a rate of 0.1 A g⁻¹ c) Cycling performance of C-TiO₂/Si and C-TiO_x/Si at 1 A g⁻¹ d) Rate capability performance of C-TiO₂/Si and C-TiO_x/Si at current densities of 0.1, 0.2, 0.5, 1, 2, 5, and 1 A g⁻¹, e) EIS spectra of C-TiO_x/Si and C-TiO₂/Si cells after 1st discharge and 100th discharge, f) The selected equivalent circuit.

TiO_x/Si cell, further confirming the hydrogenation effect on the crystalline structure, and thus electrochemical behavior of TiO₂. Another notable difference can be found between the discharge curves of the two materials. There is significant capacity contribution initiating from ~1.75 V in the C-TiO₂/Si discharge profiles, while this feature is absent in the C-TiO_x/Si discharge profiles. This phenomenon can be explained by different lithiation mechanisms with anatase TiO₂ and the largely amorphous TiO_x, which undergo a two-phase reaction and homogeneous lithiation, respectively [36]. The upper charge potential limit is lowered to 1.5 V for both cells after the fourth discharge process to avoid the repetitive lithiation/delithiation of the titanium oxide shells. In the new voltage window of 0.05–1.5 V, titanium oxide coatings remain lithiated, providing much enhanced electronic conductivity [25]. Another reason for the lowering of upper voltage limit in the half-cell testing lies in the fact that practical application requires lower anode lithiation/delithiation potentials (versus. Li/Li⁺) to provide higher overall voltages in full-cell LIBs, corresponding to higher energy densities given that same capacity is considered. Li_yTiO₂ is formed when titanium oxide is lithiated, where the y value varies according to the phase and structure of the titanium oxide used. Capacity of the C-TiO_x/

Si anode stabilizes at ~1410 mAh g⁻¹ in the first 3 cycles when the voltage window is 0.05–2.5 V and the current density is 100 mA g⁻¹, similar to that of the C-TiO₂/Si. The first-cycle CEs for C-TiO_x/Si and C-TiO₂/Si are 77.1% and 74.3%, respectively. The slight advantage of C-TiO_x/Si can be attributed to the stabilizing effect of the more robust Li_yTiO₂ shell, which promotes the formation of a passivating SEI. Capacities of those two materials are lower than that of the C/Si, which exhibits an initial charge capacity above 2100 mAh g⁻¹ (Figure S8a). This is mostly due to the higher Si content in the C/Si composite over the other two materials. After the voltage range is adjusted to 0.05–1.5 V, and the current density is maintained at 100 mA g⁻¹, capacities of both C-TiO_x/Si and C-TiO₂/Si cells drop to around 1330 mAh g⁻¹.

Cycling stability test is performed at a current density of 1 A g⁻¹ for all cells. As displayed in Fig. 3c, the initial capacities of C-TiO_x/Si and C-TiO₂/Si cells at 1 A g⁻¹ are 1075 mAh g⁻¹, and 827 mAh g⁻¹, respectively, indicating the superior capacity retaining capability of C-TiO_x/Si at an elevated current density of 1 A g⁻¹. After 200 cycles, capacity retention of 88.1% is achieved for the C-TiO_x/Si cell, with specific capacity being 938 mAh g⁻¹. In comparison, the C-TiO₂/Si cell

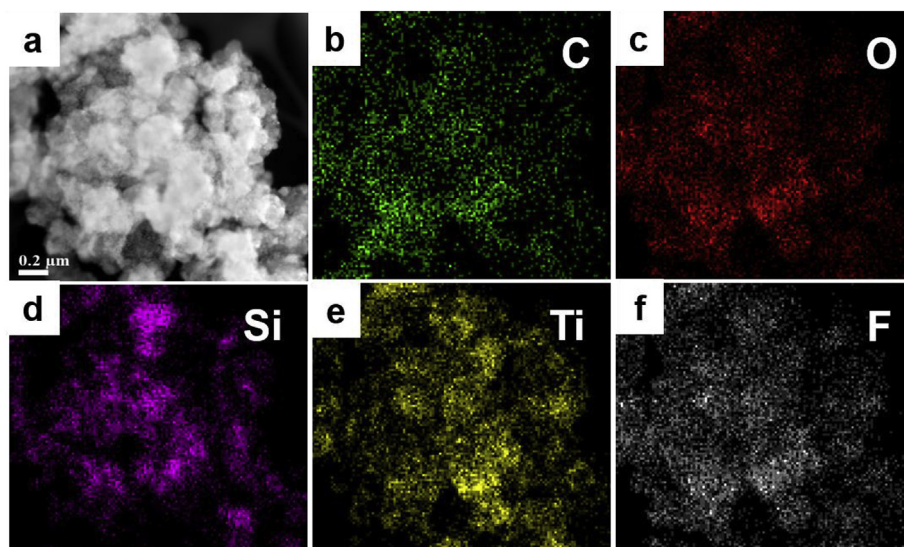


Fig. 4. a) TEM image of a C-TiO_x/Si cluster after cycling, b-f) Elemental mappings of C, O, Si, Ti, and F of the area in a), respectively.

steadily loses its capacity over cycling, with only 28.2% capacity retention after 200 cycles. As depicted in Figure S8b, the C/Si cell shows no sign of capacity decay in the first 5 cycles at a low current density of 100 mA g⁻¹. However, the cell experiences a dramatic capacity decay shortly after the cycling rate is amplified to 1 A g⁻¹. This might be caused by the poor anchoring ability of the C coating on Si surface and thus unstable C/Si structure, which cannot provide effective protection against the inevitable volume change of Si, repetitive SEI formation, and break-up of contact points between Si and the conductive network. A mere 10.8% of the original capacity is left after 150 cycles. As provided in Experimental section, all electrode fabrication parameters were maintained consistent for all electrodes. Similar mass loading and average electrode thickness of 1.8 mg cm⁻² and 21.6 μm are obtained for C-TiO₂/Si and C-TiO_x/Si electrodes, respectively, while C/Si electrodes present a lower mass loading of 1.4 mg g⁻¹ and higher thickness of 25.2 μm. Copper foil used in this work has a thickness of ~12 μm. Volumetric densities of cast electrode materials are calculated to be 1.88 g cm⁻³, and 1.06 g cm⁻³ for C-TiO_x/Si and C/Si electrodes, respectively. Considering the electrochemical performance of these electrodes, it can be concluded that the engineering of C-TiO_x coating matrix not only significantly improves cycling stability of Si, but also greatly increases the volumetric density of the electrode, contributing to enhanced energy density and prolonged durability in a LIB.

The rate performance comparison in Fig. 3d further corroborates the superior cycling stability of the C-TiO_x/Si electrode, as well as the capacity retention at elevated rates. Specific capacities of 1237, 1142, 1030, 895 and 810 mAh g⁻¹ are obtained for the C-TiO_x/Si cell at current densities of 0.2, 0.5, 1, 2 and 5 A g⁻¹, respectively. In addition, the C-TiO_x/Si cell gradually stabilizes at each amplified current density. A specific capacity of 1028 mAh g⁻¹ is achieved when the cycling rate is restored to 1 A g⁻¹, similar to the value obtained in the prior rate capability test, indicating excellent structure stability of the material after high-rate lithiation/delithiation. In contrast, the C-TiO₂/Si cell exhibits greater capacity loss over the course of all rate increments. A steady drop in capacity can be observed at each rate. The cell does not recover its capacity when the current density is reversed to 1 A g⁻¹ after rate capability test, and much worse cycling stability is observed at the subsequent cycling test compared to the C-TiO_x/Si cell. Larger capacity gaps between C-TiO_x/Si and C-TiO₂/Si graphs appear when higher rates are applied, confirming the superior rate capability of the C-TiO_x/Si electrode. The following factors regarding the materials account for the above phenomena. First, the deficiency-rich and largely amorphous nature of the TiO_x, as well as its lithiated derivatives can

provide much higher electronic conductivity over the anatase TiO₂ and the corresponding Li_yTiO₂. The amorphous TiO_x coating possesses much better elasticity and stress-release capability than the anatase TiO₂, thus can provide a more robust matrix to accommodate the volume change of Si without structural decay. Third, the uniform coating of C-TiO_x layer along with its good structural stability effectively prevents the direct and repetitive contact between Si and electrolyte, and promotes the formation of a stable SEI. The Nyquist plots analyzed from EIS data in Fig. 3e compare the C-TiO_x/Si cell and C-TiO₂/Si cell after 1st discharge and 100th discharge. The best-fitting equivalent circuit model is displayed in Fig. 3f. After the 1st discharge, two cells show similar Nyquist plot shape and Ohmic resistance R_s, indicating the consistent and highly-repeatable cell fabrication procedure. The semi-circles obtained from the high-frequency region can be interpreted as the interface (SEI and charge transfer) resistance of the electrode. The near-straight lines after semi-circles from low-frequency region stand for Li⁺ diffusion resistance of the electrode [37]. The slight difference in the diameter of two semi-circles reflects advantage of the C-TiO_x/Si cell, indicating good charge transfer in titanium oxide shell and SEI. The increase in diameter of the semi-circle in the C-TiO₂/Si plot is much smaller than that in the C-TiO_x/Si plot, which indicates a greater stability of the shell structure and the formed SEI. The fitted impedance data using model shown in Fig. 3f are displayed in Table S1.

The stable structure of the C-TiO_x/Si cluster is further evidenced by TEM and EDX elemental mapping of the cluster after 100 cycles. As shown in Fig. 4a, Si NPs remain embedded in the robust matrix of carbon and TiO_x, retaining good connectivity between active material and the secondary supporting and conductive cluster. Elemental mappings of C, O, Si, Ti, and F in Fig. 4b–f largely outline the shape of the cluster. Si mapping in Fig. 4d can be well overlapped with the Ti signals in Fig. 4e, further confirming the uniform coating and robust nature of the TiO_x shell. The structure has sufficient stability to withstand the repetitive volume change of Si, which contributes to the prolonged stable cycling of the cell. It is well known that the SEI film is typically composed of LiF, some fluorine-based polymer derived from FEC additive, and other species. Therefore, the F EDX mapping can provide a rough indication of the location of the SEI formations. Interestingly, the F map (Fig. 4f) overlaps very well with the Ti map (Fig. 4e) and also C map (Fig. 4c). In contrast, the Si map (Fig. 4d) in fact does not match up well with either F or Ti map. This suggests that the SEI preferentially forms over the protective C-TiO_x shell. This is a crucial characteristic of this material as it promotes the preferential growth of SEI on C-TiO_x layer over Si. In addition to the core-shell morphology that protects Si,

it is possible that other mechanisms might contribute to the preference. One plausible mechanism is that the relative conductive nature of C-TiO_x shell over Si can divert most electron flow through the conductive network formed by C-TiO_x, allowing for electrolyte reduction, instead of through Si. One might argue that carbon will also serve as a preferential surface for SEI growth. However, it is important to note that carbon alone is not able to withstand volume expansion of Si and maintain the structure of the original composite during cycling.

4. Conclusion

In summary, a micron-sized secondary cluster containing Si is developed via the conformal growth of a C-TiO_x coating matrix. Transformation from discrete Si NPs into micron-sized clusters significantly improves the tap density of Si and thus contribute to enhanced volumetric density of the electrode. C-TiO_x matrix with predominantly amorphous nature not only protects Si from repetitive contact with electrolyte and help form a stable SEI, but also provides a robust structure to host Si and endure the volume changes during lithiation/delithiation. Encapsulation of Si NPs into secondary clusters can effectively secure Si in the original conductive network over cycling and ensure that most Si NPs remain electrochemically active, contributing to prolonged stable cycling of the electrode. Coupled with the simple synthetic approach, the strategy proposed in this research may bear enormous practical significance for the development of commercially-viable Si anodes.

Conflicts of interest

The authors declare no conflict of interest.

Acknowledgements

This work was partially supported by Natural Sciences and Engineering Research Council of Canada (NSERC) provided to Z.C. and the University of Waterloo, General Motors Global Research and Development Centre, and the Waterloo Institute for Nanotechnology. We also appreciate Dr. Carmen Andrei from Canadian Centre for Electron Microscopy (CCEM) at McMaster University for TEM characterizations.

Appendix A. Supplementary data

Supplementary data related to this article can be found at <https://doi.org/10.1016/j.jpowsour.2018.07.082>.

References

[1] J.R. Szczech, S. Jin, *Energy Environ. Sci.* 4 (2011) 56–72.

- [2] M. Gu, Y. He, J.M. Zheng, C.M. Wang, *Nanomater. Energy* 17 (2015) 366–383.
- [3] X. Su, Q.L. Wu, J.C. Li, X.C. Xiao, A. Lott, W.Q. Lu, B.W. Sheldon, J. Wu, *Adv. Energy. Mater.* 4 (2014) 1300882.
- [4] M.T. McDowell, S.W. Lee, W.D. Nix, Y. Cui, *Adv. Mater.* 25 (2013) 4966–4984.
- [5] H. Wu, G. Chan, J.W. Choi, I. Ryu, Y. Yao, M.T. McDowell, S.W. Lee, A. Jackson, Y. Yang, L.B. Hu, Y. Cui, *Nat. Nanotechnol.* 7 (2012) 309–314.
- [6] Y.C. Yen, S.C. Chao, H.C. Wu, N.L. Wu, *J. Electrochem. Soc.* 156 (2009) A95–A102.
- [7] C.K. Chan, H.L. Peng, G. Liu, K. McIlwrath, X.F. Zhang, R.A. Huggins, Y. Cui, *Nat. Nanotechnol.* 3 (2008) 31–35.
- [8] R. Deshpande, Y.T. Cheng, M.W. Verbrugge, *J. Power Sources* 195 (2010) 5081–5088.
- [9] T. Song, J.L. Xia, J.H. Lee, D.H. Lee, M.S. Kwon, J.M. Choi, J. Wu, S.K. Doo, H. Chang, W. Il Park, D.S. Zang, H. Kim, Y.G. Huang, K.C. Hwang, J.A. Rogers, U. Paik, *Nano Lett.* 10 (2010) 1710–1716.
- [10] D.S.M. Iaboni, M.N. Obrovac, *J. Electrochem. Soc.* 163 (2016) A255–A261.
- [11] K. Feng, M. Li, W. Liu, A.G. Kashkooli, X. Xiao, M. Cai, Z. Chen, *Small* 14 (2018) 1702737.
- [12] A. Casimir, H. Zhang, O. Ogoke, J.C. Amine, J. Lu, G. Wu, *Nanomater. Energy* 27 (2016) 359–376.
- [13] J.-Y. Li, Q. Xu, G. Li, Y.-X. Yin, L.-J. Wan, Y.-G. Guo, *Mater. Chem. Front.* 1 (2017) 1691–1708.
- [14] Y. Jin, B. Zhu, Z. Lu, N. Liu, J. Zhu, *Adv. Energy. Mater.* 7 (2017) 1700715.
- [15] S. Chae, M. Ko, K. Kim, K. Ahn, J. Cho, *Joule* 1 (2017) 47–60.
- [16] M. Li, Y.N. Zhang, F. Hassan, W. Ahn, X.L. Wang, W.W. Liu, G.P. Jiang, Z.W. Chen, *J. Mater. Chem.* 5 (2017) 21435–21441.
- [17] K. Feng, W. Ahn, G. Lui, H.W. Park, A.G. Kashkooli, G. Jiang, X. Wang, X. Xiao, Z. Chen, *Nanomater. Energy* 19 (2016) 187–197.
- [18] Y. Liu, Y.F. Yang, *J. Nanomater.* (2016) 15.
- [19] Y.Y. Zhang, Y.X. Tang, W.L. Li, X.D. Chen, *Chemnanomat* 2 (2016) 764–775.
- [20] Y. Tang, Y. Zhang, J. Deng, J. Wei, H.L. Tam, B.K. Chandran, Z. Dong, Z. Chen, X. Chen, *Adv. Mater.* 26 (2014) 6111–6118.
- [21] Q.L. Wu, T. Tran, W.Q. Lu, J. Wu, *J. Power Sources* 258 (2014) 39–45.
- [22] J. Brumberov, J. Kunze-Liebhauser, *J. Power Sources* 258 (2014) 129–133.
- [23] W. Luo, Y.X. Wang, L.J. Wang, W. Jiang, S.L. Chou, S.X. Dou, H.K. Liu, J.P. Yang, *ACS Nano* 10 (2016) 10524–10532.
- [24] F. Maroni, G. Carbonari, F. Croce, R. Tossici, F. Nobili, *Chemsuschem* 10 (2017) 4771–4777.
- [25] E.M. Lotfabad, P. Kalisvaart, K. Cui, A. Kohandehghan, M. Kupsta, B. Olsen, D. Mitlin, *Phys. Chem. Chem. Phys.* 15 (2013) 13646–13657.
- [26] M.L. Sushko, K.M. Rosso, J. Liu, *J. Phys. Chem. C* 114 (2010) 20277–20283.
- [27] G. Jeong, J.G. Kim, M.S. Park, M. Seo, S.M. Hwang, Y.U. Kim, Y.J. Kim, J.H. Kim, S.X. Dou, *ACS Nano* 8 (2014) 2977–2985.
- [28] S.J. Park, Y.J. Kim, H. Lee, *J. Power Sources* 196 (2011) 5133–5137.
- [29] J.P. Yang, Y.X. Wang, W. Li, L.J. Wang, Y.C. Fan, W. Jiang, W. Luo, Y. Wang, B. Kong, C. Selomulya, H.K. Liu, S.X. Dou, D.Y. Zhao, *Adv. Mater.* 29 (2017) 1700523.
- [30] R. Ren, Z. Wen, S. Cui, Y. Hou, X. Guo, J. Chen, *Sci. Rep.* 5 (2015) 10714.
- [31] J.-Y. Eom, S.-J. Lim, S.-M. Lee, W.-H. Ryu, H.-S. Kwon, *J. Mater. Chem.* 3 (2015) 11183–11188.
- [32] M. Mehta, N. Kodan, S. Kumar, A. Kaushal, L. Mayrhofer, M. Walter, M. Moseler, A. Dey, S. Krishnamurthy, S. Basu, A.P. Singh, *J. Mater. Chem.* 4 (2016) 2670–2681.
- [33] M.Y. Wu, J.E.C. Sabisch, X.Y. Song, A.M. Minor, V.S. Battaglia, G. Liu, *Nano Lett.* 13 (2013) 5397–5402.
- [34] S. Chae, M. Ko, S. Park, N. Kim, J. Ma, J. Cho, *Energy Environ. Sci.* 9 (2016) 1251–1257.
- [35] G.F. Ortiz, I. Hanzu, T. Djenizian, P. Lavela, J.L. Tirado, P. Knauth, *Chem. Mater.* 21 (2009) 63–67.
- [36] H. Bin Wu, X.W. Lou, H.H. Hng, *Chem. Eur J.* 18 (2012) 3132–3135.
- [37] H.J. Tian, X.J. Tan, F.X. Xin, C.S. Wang, W.Q. Han, *Nanomater. Energy* 11 (2015) 490–499.